Electronic Supplementary Information

Supramolecular interaction of molecular catalyst on a polymeric carbon nitride photoanode enhances photoelectrochemical activity and stability at neutral pH

Sanjit Mondal,‡[a] Martina Salati,‡[b],[c] Marco Nicaso,[b],[c] Josep Albero,[d] Mireia Segado-Centellas,[b] Michael Volokh,[a] Carles Bo,*[b] Hermenegildo García,[d] Marcos Gil-Sepulcre,*[b] Antoni Llobet,*[b],[e] Menny Shalom*[a]

[a] Department of Chemistry and Ilse Katz Institute for Nanoscale Science and Technology, Ben-Gurion University of the Negev, Beer-Sheva 8410501, Israel.

Corresponding author E-mail: mennysh@bgu.ac.il

[b] Institute of Chemical Research of Catalonia (ICIQ), Barcelona Institute of Science and Technology (BIST) Av. Països Catalans 16, Tarragona 43007, Spain.
Corresponding author E-mail: cbo@iciq.cat, mgil@iciq.cat, allobet@iciq.cat

[c] Universitat Rovira i Virgili Av. Països Catalans 35, Tarragona 43007, Spain.

[d] Instituto Universitario de Tecnología Química CSIC-UPV, Universitat Politècnica de València, València 46022, Spain.

[e] Departament de Química, Universitat Autònoma de Barcelona Cerdanyola del Vallès, Barcelona 08193, Spain.

‡ Equal contribution.

Materials:

All mentioned chemicals were purchased from commercial sources and used directly without further purification. Thiourea (99%) was brought from Acros Organics. Sodium sulphate anhydrous (Na_2SO_4, 99%) was purchased from Loba Chemie, India. Melamine (99%) and 2,2,2-trifluoroethanol (TFE, 99%) were brought from Sigma-Aldrich. Disodium phosphate (Na_2HPO_4 ,98+%) and sodium dihydrogen phosphate (NaH_2PO_4, 96%) were purchased from Alfa Aesar. Ethanol (≥99%), and acetone (≥99%) were brought from Bio-Lab Ltd, Israel. For the synthesis of Ru based complexes, all the chemicals used in this work were provided by Sigma Aldrich, unless explicitly indicated. $RuCl_3{\cdot}xH_2O$ was purchased from Alfa Aesar. The precursor complexes $[RuCl_2(dmso)_4]$ and $[Ru(tda)(dmso)(H_2O)]$ and also 6,6′-dicarboxylic acid-[2,2′:6′,2′′-terpyridyl] (H_2tda) were prepared according to a reported procedure.[1] Fluorine-doped tin oxide (FTO)-coated glass (12–14 Ω sq^{-1}) was purchased from Xop Glass company, Spain. deionized water using Millipore Milli Q Direct 3 purification system (18.2 MΩ cm resistivity at room temperature) was used for all the experiments.

Characterization:

The structural analysis of synthesized films was carried out using X-ray diffraction patterns (XRD), using a PANalytical's Empyrean diffractometer equipped with a position sensitive detector X'Celerator. XRD data was recorded with a scanning time of ~7 min for 2ϑ ranging from 5° to 60° using Cu Kα radiation (λ = 1.54178 Å, 40 kV, 30 mA). X-ray photoelectron spectroscopic (XPS) data were obtained from an X-ray photoelectron spectrometer ESCALAB 250 ultrahigh vacuum (1×10^{-9} bar) device with an Al Kα X-ray source and a monochromator. The X-ray beam size was 500 µm. All spectra were calibrated relative to a carbon C 1s peak, positioned at 284.8 eV, to correct the charging effect. To study the materials' functional groups, Fourier-transform infrared spectroscopy (FTIR, Thermo Scientific Nicolet iS5 FTIR spectrometer equipped with a Si ATR) was used. UV–vis diffuse reflectance spectroscopy (DRS, on Cary 100 spectrophotometer, equipped with a diffuse reflectance accessory), photoluminescence spectroscopy (Horiba Scientific FluroMax 4 spectrofluorometer), and time-correlated single photon counting measurements (Edinburgh Instruments LifeSpec II spectrometer) were performed to study their optical properties. The excitation wavelength (λ_{ex}) was 370 nm and the emission wavelength (λ_{em}) was 460 nm. The acquisition was carried out fixing the maximum number of emission counts to 5×10^3 and the measurements were carried out under ambient condition. Morphology of the CN films were characterized by scanning electron microscopy (SEM) using a FEI Verios high-resolution SEM, which is equipped with a FEG source and a through-lens detector (secondary electrons) operated at U_0 = 3.5 kV and I = 25 pA. Energy dispersive X-ray spectrometry (EDS) data were obtained using a FEI Verios 460L high resolution SEM equipped with a FEG source and operated at U_0 = 20 kV. HAADF-STEM images were recorded using S/TEM Spectra 200

microscope. Bruker Avance 500 MHz instruments were used to carry out NMR spectroscopy. 20 mg of powder of **CN_{TM}–Ru_{15}** sample (corresponding to 1 cm^2 area) were digested in 10 mL of aqueous solution with 7% HCl and analyzed at the ICP-OES using a Spectro ARCOS ICP-OES, FHX22 multi-view plasma instrument. The analysis was repeated three times.

PEC and electrochemical measurements: All the photoelectrochemical measurements were performed using a three-electrode configuration system on a PalmSens3 potentiostat (PalmSens, Netherlands). A Pt foil (1.0 cm^2) and Ag/AgCl (saturated KCl) were used as the counter- and reference-electrode, respectively. Phosphate buffer solution, (pH ~7) 0.1 M was used as the electrolyte for the photocurrent measurements. The photoanode was dipped into electrolyte medium in a custom-made PTFE cell. The obtained potentials were converted to the reversible hydrogen electrode (RHE) scale using Equation S1:

$$V_{RHE} = V_{Ag/AgCl} + 0.0591 \times pH + 0.197 \quad \text{(S1)}$$

Photocurrents were recorded at a bias of 1.23 V vs. RHE using illumination from a solar simulator (Newport 300 W ozone-free Xe arc lamp, equipped with water and air mass AM 1.5G filters). 1 sun illumination was calibrated by means of a silicon photodiode (Newport power meter model 919-P) providing a 100 mW cm^{-2} power density to the photoelectrode. For incident photon-to-current conversion efficiency (IPCE) measurement a Zahner CIMPS-QE/IPCE photoelectrochemical workstation coupled with a TLS03 tunable light source controlled by a PP211 potentiostat (Zahner-Elektrik, Germany) in a dedicated three-electrode photoelectrochemical cell (PEEC-2) using an Ag/AgCl (sat. KCl) reference electrode and Pt coil as the counter electrode. For incident photon-to-current conversion efficiency (IPCE) measurement the following Equation S2 was used:

$$\text{IPCE}\ (\%) = \frac{J\left(\text{mA cm}^{-2}\right) \cdot 1240\ (\text{V nm})}{\lambda(\text{nm}) \cdot I_{\text{incident}}(\text{mW cm}^{-2})} \times 100\% \quad \text{(S2)}$$

Where j is the photocurrent density, λ is the illumination wavelength, $I_{incident}$ (calibrated to illumination spot of 8 mm in diameter) is the incident illumination power, and 1240 is the unit conversion factor. The calculation was performed by the coupled ThalesXT software.

All electrochemical measurements were performed using a three-electrode system on an Autolab potentiostat (Metrohm, PGSTAT302N). 0.5 M Na_2SO_4 aqueous solution was used for impedance spectroscopy measurement. Nyquist plots of the films were measured at an applied potential of 1.23 V vs. RHE with a frequency range from 40 kHz to 100 mHz and a 5 mV amplitude of the sinusoidal perturbation. The O_2 production for **CN_{TM}** and **CN_{TM}–Ru_{15}** film in phosphate buffer solution (pH ~7) was detected using a fiber optic oxygen meter under chronoamperometric condition (1.23 V vs. RHE, 1 sun illumination). A two-compartment cell (H-cell) was used and tightly sealed with a rubber septum for each chamber and parafilm to avoid any gas leakage. The electrolyte solution was purged with Ar for 30 min before the experiments. The

O_2 quantification was performed for the duration of 1 hour, as shown in Fig. S6. FE was calculated using Equations S3 and S4:

$$n = \frac{I \cdot t}{z \cdot F} \tag{S3}$$

$$\mathrm{FE}(\%) = \frac{\text{Experimental } \mu\text{mol of } O_2}{\text{Theoretical } \mu\text{mol of } O_2} \times 100\% \tag{S4}$$

Where *n* is the O_2 amount (measured in mol), *I* stands for the current (A), *z* is the number of transferred electrons (for O_2 evolution, *z* = 4), *t* is the time (s), and *F* is the Faraday constant (96485 C mol^{-1}).

Preparation of the CN photoelectrodes (CN_{TM}):

CN films were prepared using an adapted procedure,[2,3] using thiourea as the precursor material. Typically, 40 g thiourea was dissolved in a 100 mL glass beaker containing 40 mL DI water, and this solution was heated and stirred for 1 h at 85 °C at a constant stirring rate of 300 rpm using a PTFE-coated magnetic stir bar to reach finally a saturated aqueous thiourea solution. In the next step, a clean FTO was dipped into the hot saturated thiourea solution, resulting in a uniform precursor film layer on FTO after the remaining attached solution is left to dry. This dip-dry process was repeated for three times to increase the thickness. Next, thiourea-coated FTOs were dried at 70 °C for 1 h on a hot plate and transferred into a glass test-tube containing 1 g of melamine powder at its bottom. The test-tubes were wrapped tightly with aluminum foil and calcined at the target temperature of 500 °C for 2 h under nitrogen (N_2) atmosphere in a tube furnace (heating ramp from room temperature to the target temperature of 5 °C min^{-1}).

Preparation of [Ru(tda)(4,4'-bpy)]$_{15}$(4,4'-bpy) oligomer (Ru_{15}):

The final [Ru(tda)(4,4'-bpy)]$_{15}$(4,4'-bpy) oligomer, as well as the ligand 6,6'-dicarboxylic acid-[2,2':6',2''-terpyridyl] (H_2tda) and the precursor complexes [$RuCl_2(dmso)_4$] and [Ru(tda)(dmso)(H_2O)], were synthesized according to the literature.[1,4]

Functionalization of [Ru(tda)(4,4'-bpy)]$_{15}$(4,4'-bpy) oligomer on CN photoelectrodes (CN_{TM}-Ru_{15}):

For the loading of the [Ru(tda)(4,4'-bpy)]$_{15}$(4,4'-bpy) oligomer onto the **CN_{TM}** electrodes surface, 1 mg of the **Ru_{15}** was dissolved in 10 mL TFE solvent and CN photoanodes were thus completely soaked in the orange-reddish oligomer solution for 20 minutes, and afterwards rinsed with clean TFE solvent to remove the excess Ru-complex which does not interact with the CN. The modified CN electrodes (labelled as **CN_{TM}–Ru_{15}**) were finally dried at 70 ℃ on a hot plate for 60 min, before using them for photoelectrochemical experiments.

Computational details:

The geometric parameters of all molecular structures were fully optimized at a density functional theory (DFT) level using the software package AMS2021.[5] The molecular geometries were computed using the BP86-D3 density functional combined method (Becke exchange functional[6] with gradient correction provided by the Perdew expression,[7] plus Grimme's D3 empirical dispersion correction).[8] Slater type DZP basis set for elements H, C, N, and O, and TZP basis set for the Ru were used as provided in the ADF library. ZORA[9,10] scalar relativistic corrections were also included. The COSMO[11,12] implicit solvation model was selected to simulate the aqueous solvation effects. The band gap was finally evaluated through single point calculations with the HSE06 functional.[13] The electron absorption energies were computed by using TD-DFT with the statistical average of orbital potentials (SAOP)[14,15] exchange-correlation functional. The spectra were simulated using a gaussian sum with 35 nm, 150 nm, and 150 nm bandwidth for Ru oligomer, carbon nitride, and the anchored system, respectively. The number of excitations included in the TD-DFT calculation was 150 for Ru oligomer and carbon nitride, and 500 for the anchored system. All the structures and output files were uploaded to the ioChem-BD database[16] and are openly accessible.

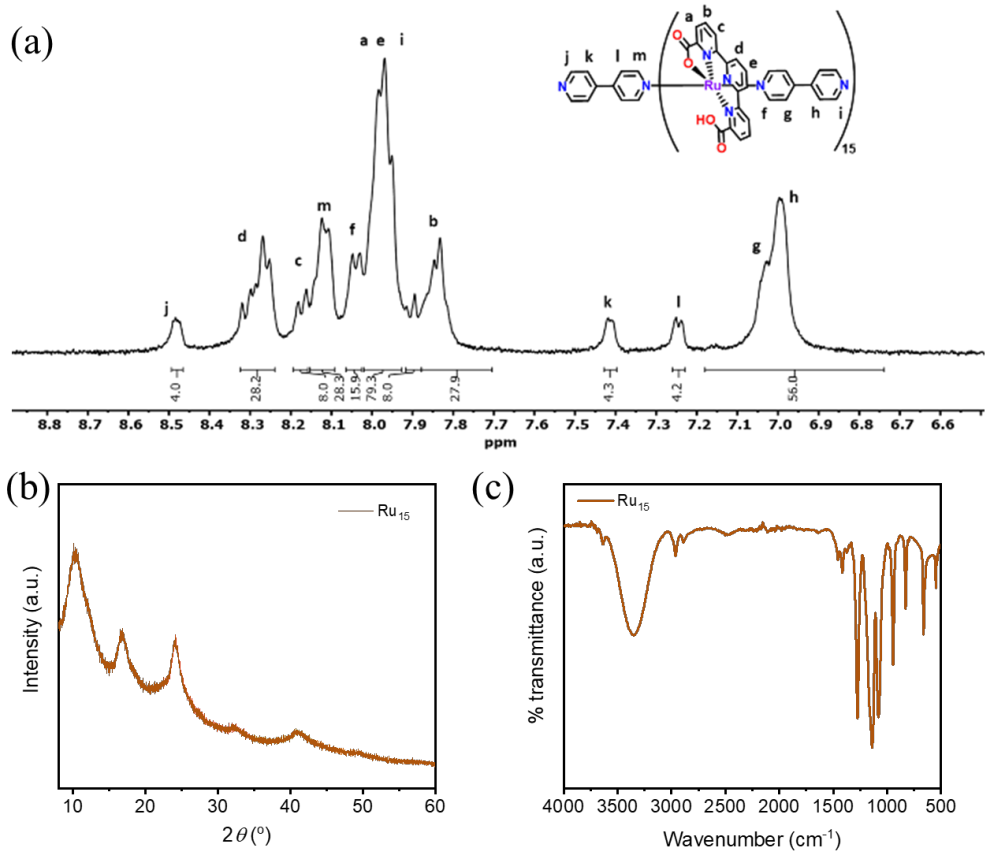

Fig. S1. Ru_{15} oligomer analysis. (a) ^{1}H NMR spectrum (500 MHz, 298 K, [d_2]-DCM/[d_3]-TFE (4:1)), (b) XRD patten, and (c) FTIR spectrum.

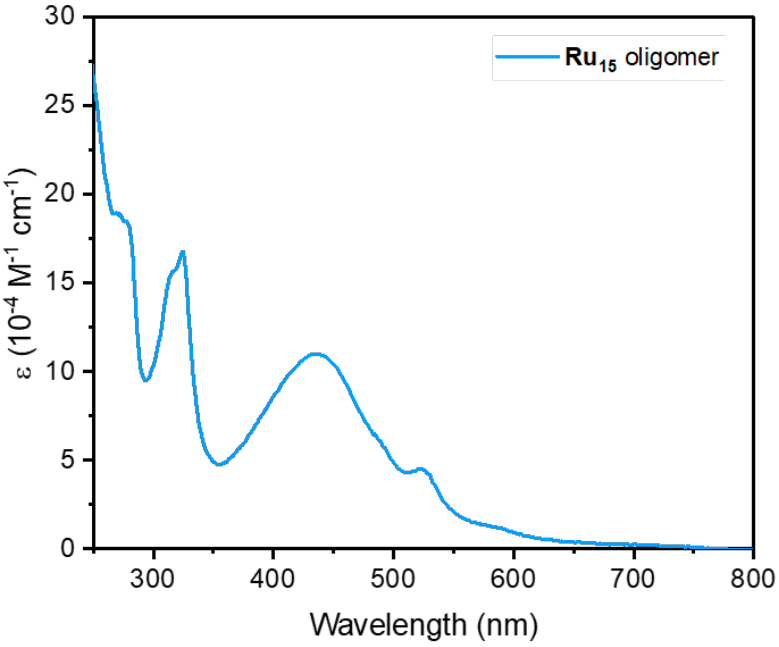

Fig. S2. UV–vis absorption spectrum of **Ru_{15}** oligomer (2 mM in TFE).

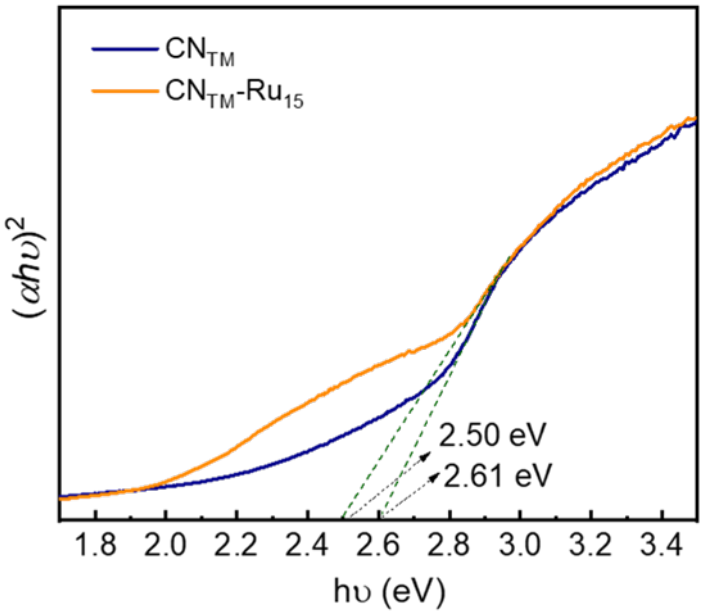

Fig. S3. Tauc plot calculation, using UV–vis diffuse reflectance spectra of **CN_{TM}** and **CN_{TM}–Ru_{15}** films, with the respective energy band gap (E_g), assuming a direct E_g.

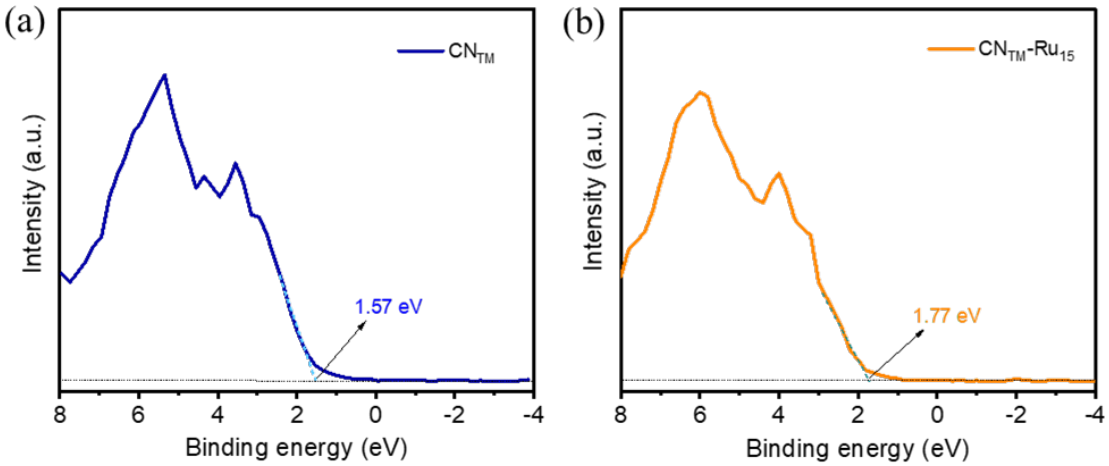

Fig. S4. Valence band (VB) XPS spectra of (a) **CN_{TM}**, (b) **CN_{TM}–Ru_{15}** films, respectively.

To convert the measured XPS VB values of the photoanodes to the normal hydrogen electrode (NHE) scale, the following calculation was performed (Eq. S5):

$$E_{NHE}\ (V) = \Phi + E_{VB\text{-}XPS} - 4.44 \qquad (S5)$$

Where Φ is the work function of the instrument (Φ = 4.84 eV), $E_{VB\text{-}XPS}$ is the measured valence band maximum energy value, and 4.44 eV is the vacuum level.[17]

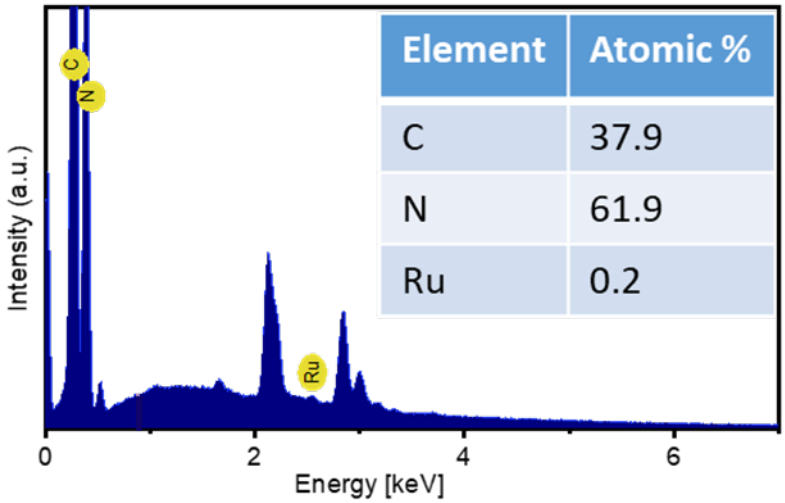

Fig. S5. Energy-dispersive X-ray spectroscopy (EDS) of **CN_{TM}–Ru_{15}** film. The EDS was carried out coupled to an SEM instrument, operated at U_0 = 10 kV on a film without sputtering. The indicated Ru peak represents the Lα edge ca. 2.56 keV.

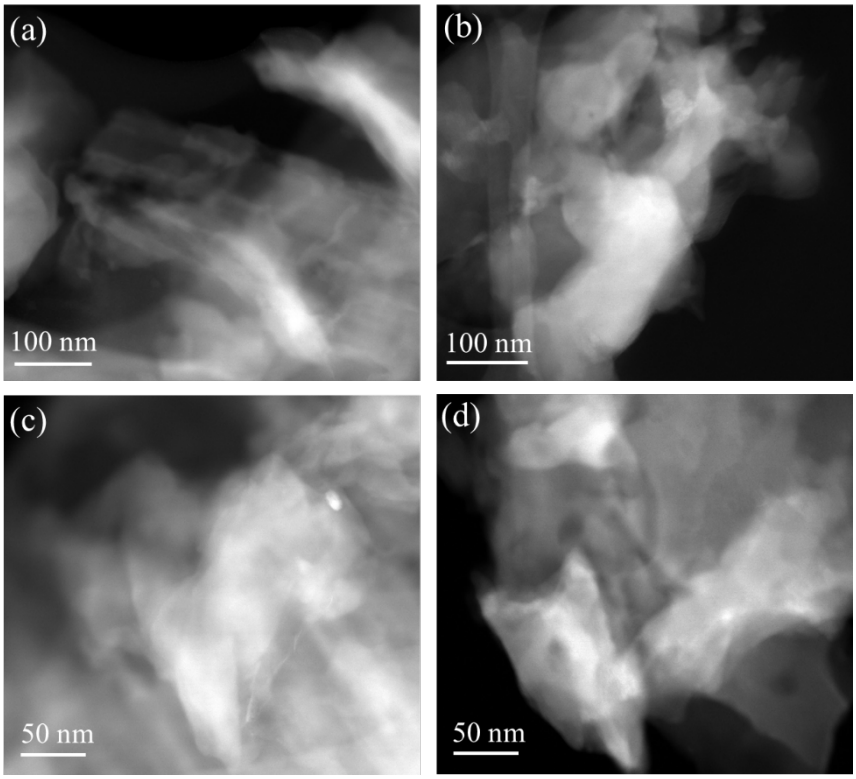

Fig. S6. (a–d) HAADF STEM images of a **CN_{TM}–Ru_{15}** sample.

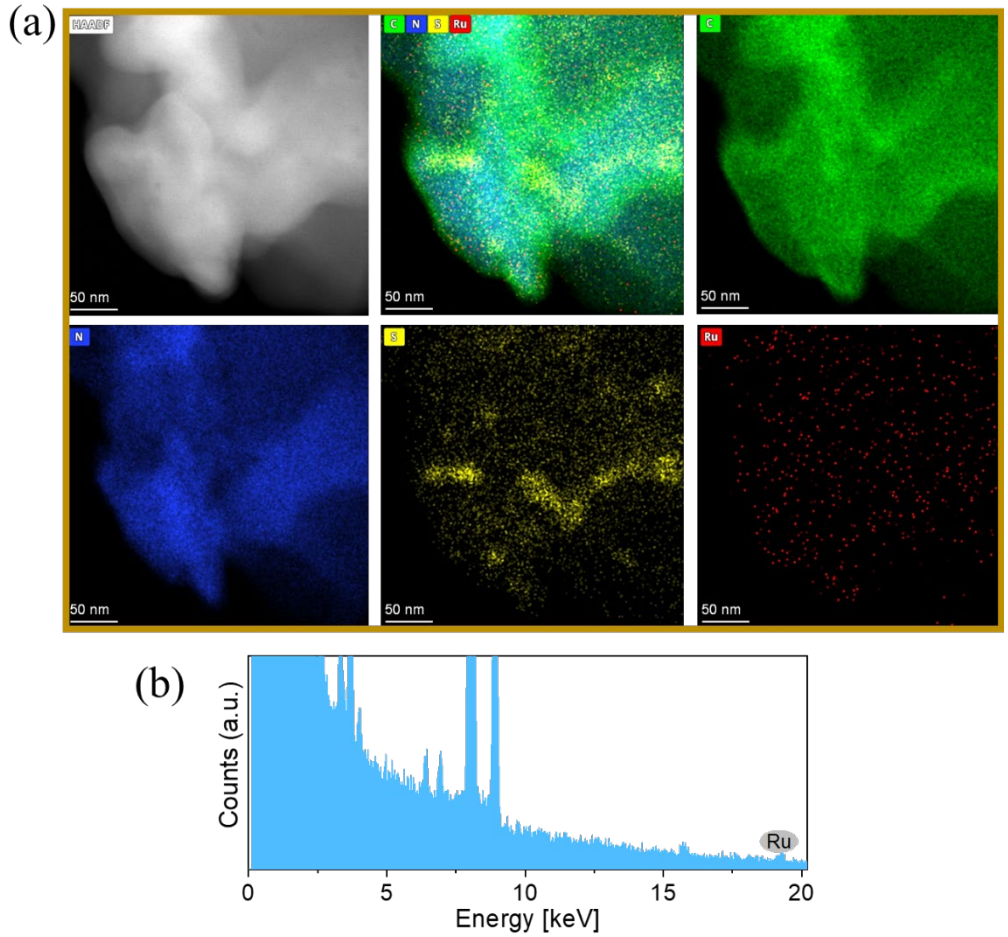

Fig. S7. (a) EDS mapping of a **CN_{TM}–Ru_{15}** sample showing a HAADF STEM image, a combined elemental map, and maps of four individual elements—carbon in green, nitrogen in blue, sulfur in yellow, and ruthenium in red. (b) EDS spectrum of **CN_{TM}–Ru_{15}** sample showing the Ru Kα edge ca. 19.2 keV.

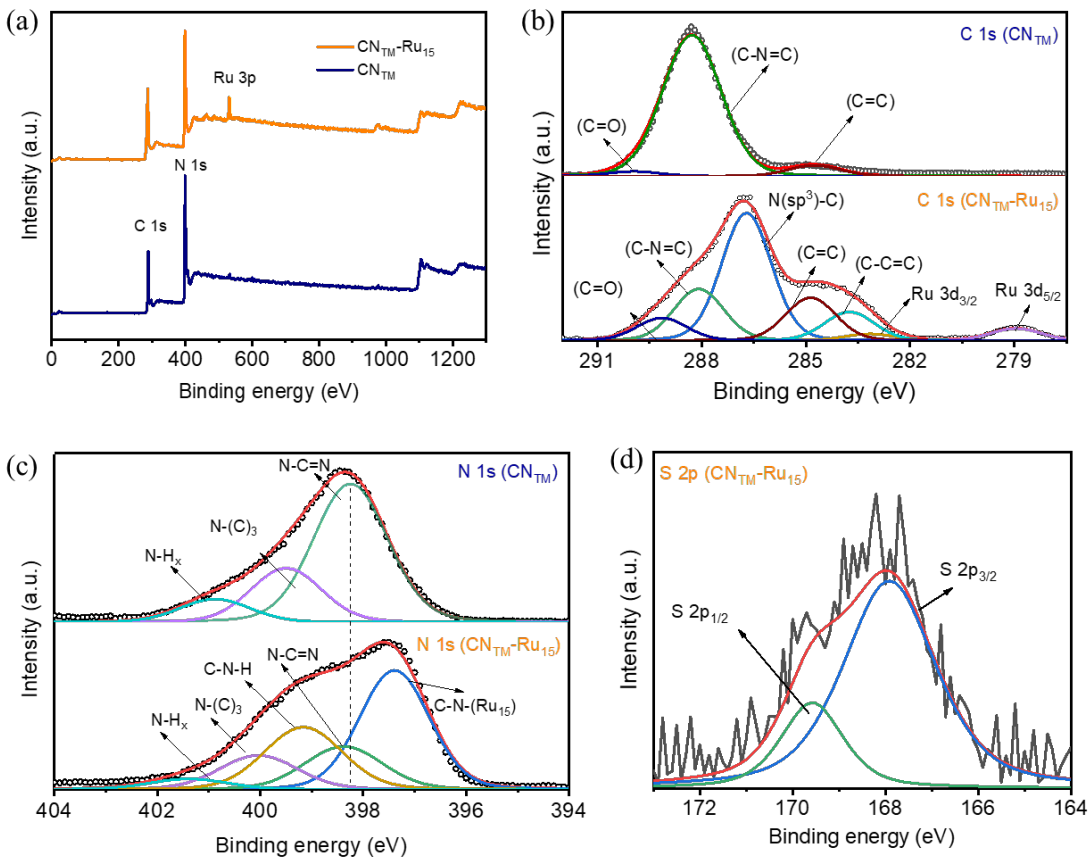

Fig. S8. XPS analysis of **CN_{TM}** and **CN_{TM}–Ru_{15}** films. (a) XPS survey spectra. (b) High-resolution C 1s XPS spectra. (c) High-resolution N 1s XPS spectra. (d). High-resolution S 2p XPS spectrum of **CN_{TM}–Ru_{15}** film.

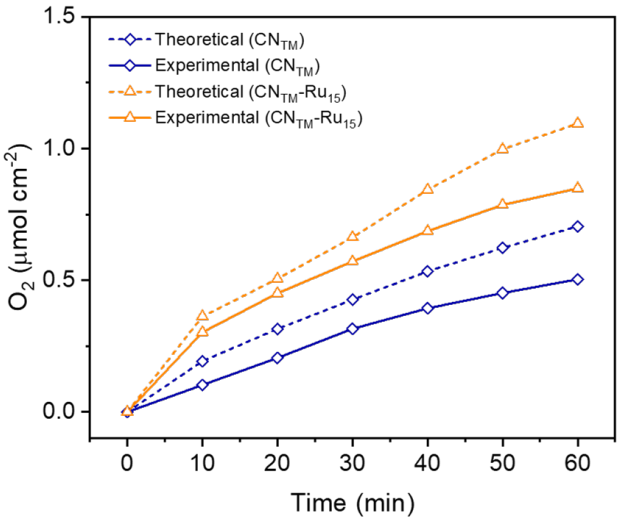

Fig. S9. Amount of O_2 produced over time using a **CN_{TM}–Ru_{15}** photoanode (orange solid line) in a phosphate buffer (pH 7, 0.1 M) at 1.23 V_{RHE} under 1 sun illumination with respect to **CN_{TM}** blank (blue solid line). The theoretical amount of O_2 for **CN_{TM}** (blue dotted line) and **CN_{TM}–Ru_{15}** (orange dotted line) is also shown, calculated from Equation S3 (Electronic Supplementary Information, detailed experimental section, PEC and electrochemical measurements subsection).

Table S1. Amount of Ru metal found by ICP-OES in **CN_{TM}–Ru_{15}** samples.

Amount sample analyzed (mg) [a]	Amount Ru obtained (mg L^{-1})	µg (Ru) g^{-1} (sample) [b]	% Ru	nmol (Ru) g^{-1} (sample)
20	0.013	6.5	6.5 x 10^{-4}	64.3

[a] The amount of sample analyzed (20 mg) corresponds to the area irradiated of the electrode (1 cm^2). [b] The transformation from mg L^{-1} to µg Ru g^{-1} sample was performed considering the amount of sample analyzed and the volume of digested solution injected (10 mL).

Table S2. Calculated TON and TOF from the O_2 evolution experiments.

	µmol O_2 cm^{-2} min^{-1}	Time (min)	Total O_2 amount (µmol)	FE (%)[a]	TON[b]	TOF (h^{-1})[c]
CN_{TM}	8.4×10^{-3}	60	0.5	74	—	—
CN_{TM}–Ru_{15}	0.014	60	0.85	89.3%	660	1409

[a] The Faradaic efficiency reported was calculated after 20 min of experiment, representing the maximum value that was reached during the measurement, comparing experimental and theoretical data. [b] The value of TON was calculated considering the total amount of O_2 produced in mol, divided by the mol of Ru found through ICP-OES. [c] The value of TOF was calculated considering the total amount of O_2 produced in mol, divided by the mol of Ru found through ICP-OES and the time (in hours) when the rate of O_2 production is faster (10 min).

Table S3. Comparison of different CN photoanodes used with water oxidation catalysts for OER.

Entry	Material	Electrolyte	Photocurrent (μA cm^{-2}) at 1.23 V vs RHE	Faradaic efficiency (%)	Light intensity	Ref.
1	**CN_{TM}**	0.1 M Na_2HPO_4/NaH_2PO_4, pH 7	130 ± 10		100 mW cm^{-2} AM 1.5 G	This work
2	**CN_{TM}–Ru_{15}**	0.1 M Na_2HPO_4/NaH_2PO_4, pH 7	180 ± 10	89.3	100 mW cm^{-2} AM 1.5 G	This work
3	CN-MR/$NiFeO_xH_y$	0.1 M KOH, pH 13	320 ± 28	43.8	100 mW cm^{-2} AM 1.5 G	18
4	CoPOM-PEI-CN_x-TiO_2	0.1 M borate solution, pH 8	230	15 ±4	λ > 420 nm, 150 mW cm^{-2}	19
5	Ni-CN_x	0.1 M aqueous KOH, pH ~ 13	69.8	—	100 mW cm^{-2} AM 1.5 G	20
6	3DB WO_3-NA/C_3N_4-NS//CoO_x	0.01 M Na_2SO_4	1.5×10^3	82.8	150 mW cm^{-2} AM 1.5 G	21

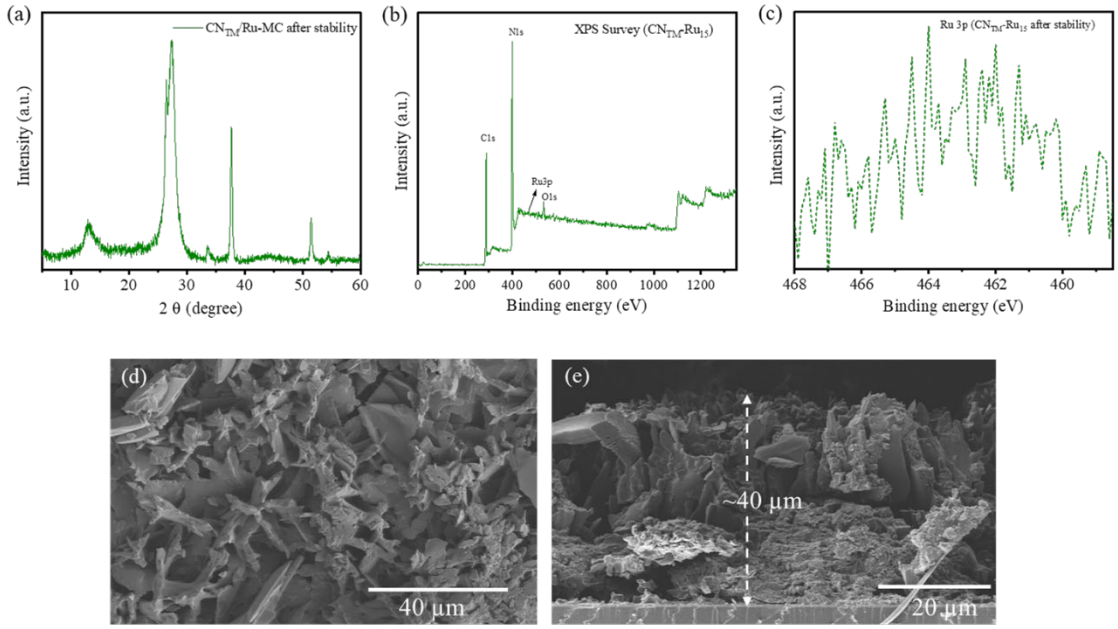

Fig. S10. Characterization of **CN_{TM}–Ru_{15}** films after the stability measurement. (a) XRD, (b) XPS survey spectrum, (c) High-resolution Ru 3p XPS spectrum, and SEM images: (d) Top-view and (e) cross-section.

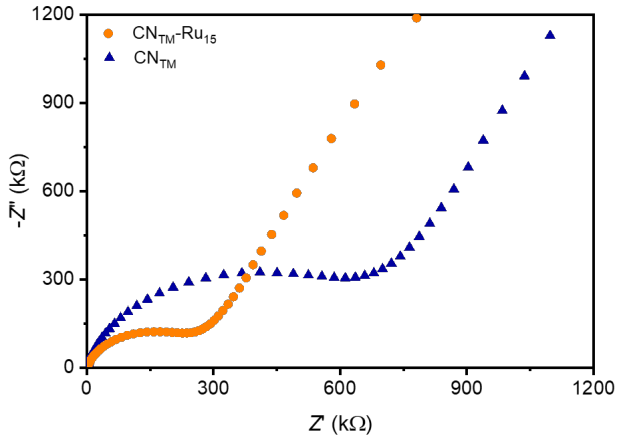

Fig. S11. Nyquist plot (raw data) from EIS measurement of **CN$_{TM}$** and **CN$_{TM}$–Ru$_{15}$** films (the fitted data and equivalent circuit are shown in Fig. 4e).

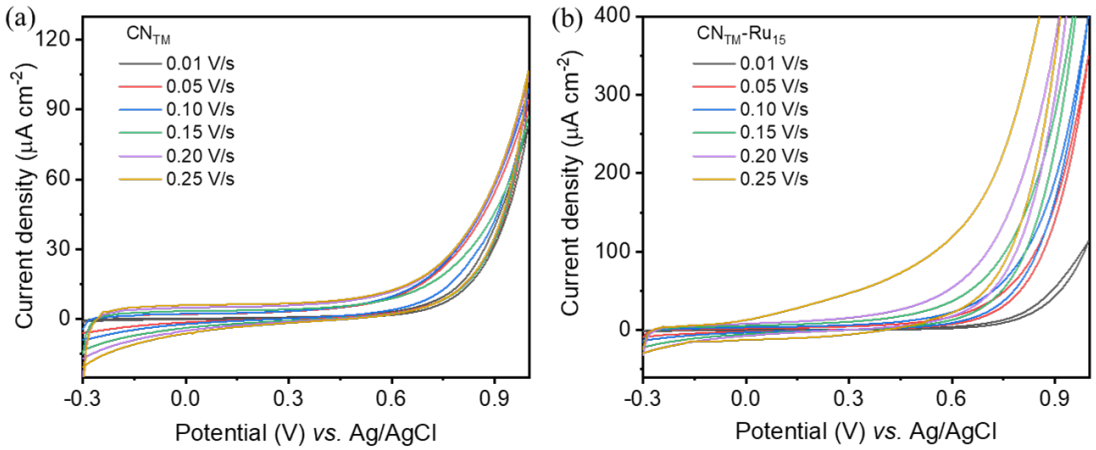

Fig. S12. Cyclic voltammetry test of the **CN$_{TM}$** and **CN$_{TM}$–Ru$_{15}$** films as a function of scan rate.

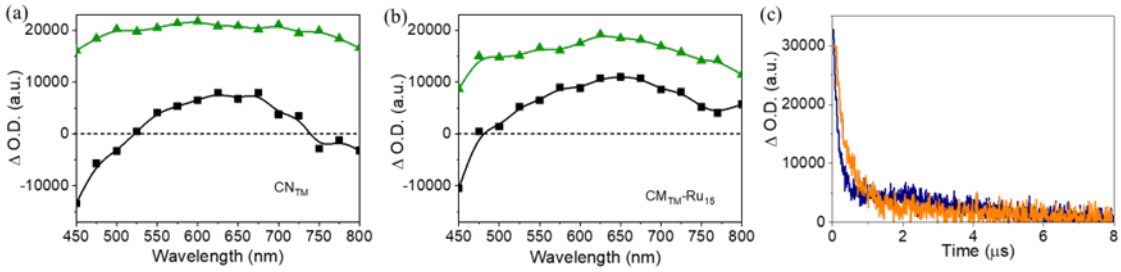

Fig. S13. Transient absorption spectra of (a) **CN_{TM}** and (b) **CN_{TM}–Ru_{15}** dispersions in acetonitrile (black squares) or 2:1 v/v acetonitrile:MeOH mixture (green triangles) acquired at 250 ns under N_2 atmosphere upon 355 nm laser excitation. (c) Transient absorption decay of **CN_{TM}** (blue) and **CN_{TM}–Ru_{15}** (orange) dispersions in 7:3 v/v acetonitrile:MeOH mixture, monitored at 650 nm under N_2 atmosphere upon 355 nm laser excitation.

Structure optimization and anchoring:

A dimer of Ru(tda) connected by a 4,4'-bpy and a carbon nitride of 164 atoms (60 C, 86 N, 18 H) were used to study the oligomer attachment onto the surface. Initially, the geometries of carbon nitride and dimer were optimized separately. These structures were later used for the anchoring analysis.

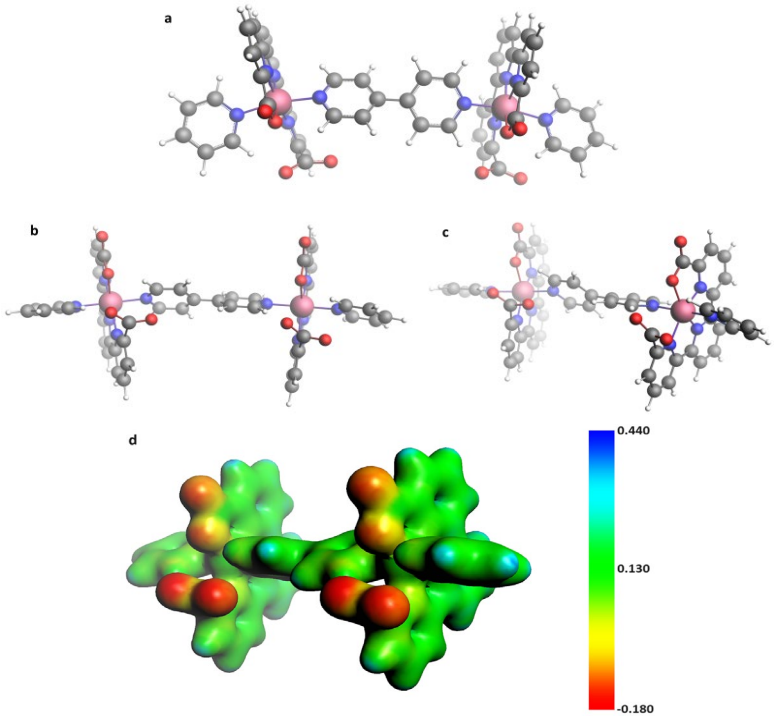

Fig. S14. Optimized molecular structures of Ru(tda)py_2 dimer; (a) top view, (b) front view, (c) side view, (d) molecular electrostatic potential map (a.u.).

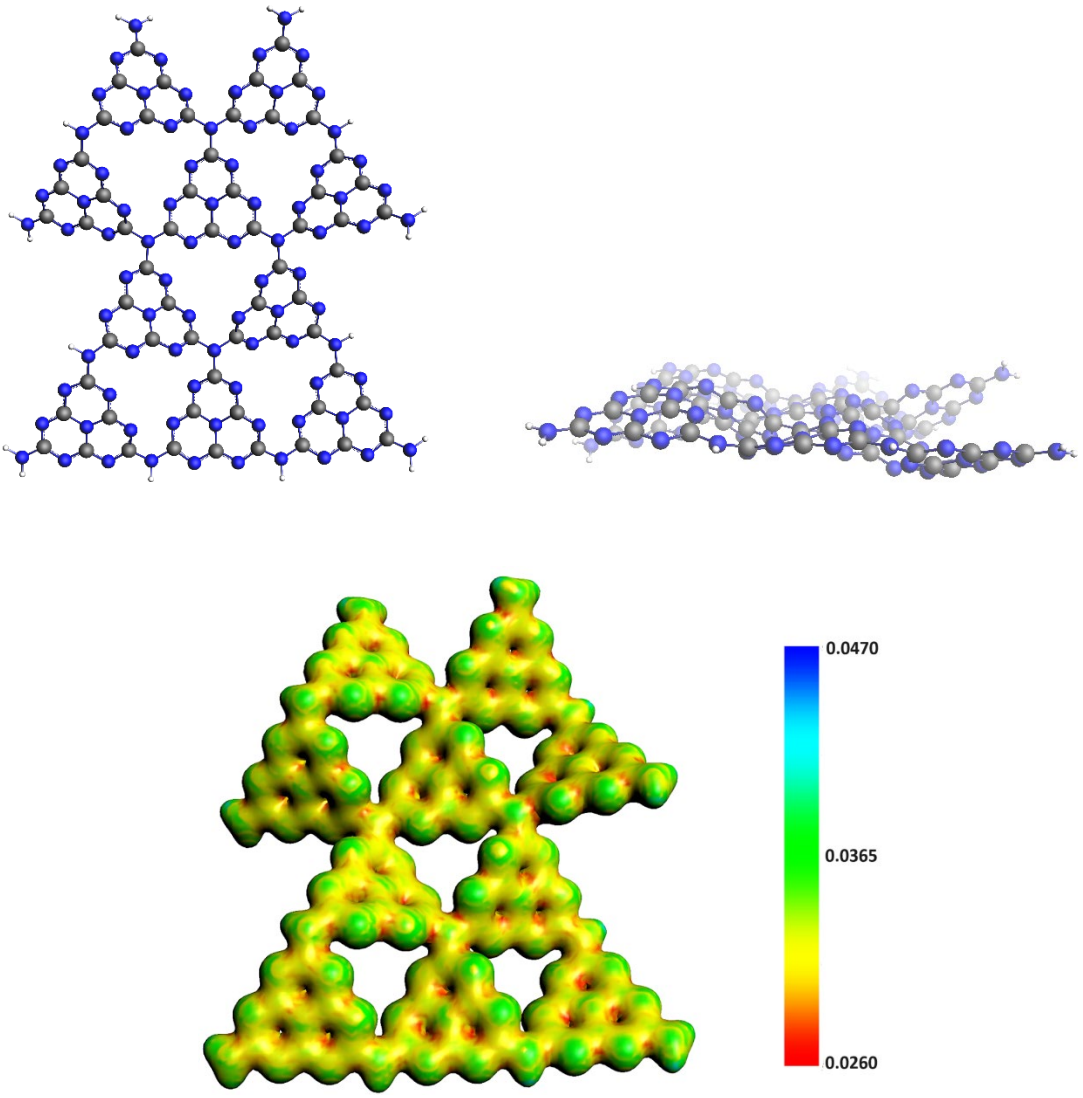

Fig. S15. Optimized structure of carbon nitride surface; top view (top left), side view (top right), and molecular electrostatic potential map (a.u., bottom).

The optimized structure of the carbon nitride results to be non-planar as previous studies have suggested by comparing experimental data and computational.[22,23] Further details regarding the carbon nitride structure are presented in the section **Carbon nitride structure insights**.

Moreover, the band gap of the material was determined using the HSE06 functional, which yields more suitable outcomes for simulating such electronic properties.[24,25] A larger model consisting of a two-layer of carbon nitride was required to replicate the electronic structure of the solid (see Fig. 1). The resulting computed value of 2.62 eV agrees with the measured value (2.61 eV).

In this study, the complex and the carbon nitride surface were assembled with different relative orientations and the different starting geometries were left to adjust to their energy minima. This method permitted obtaining five different stable attachments. The five geometries were labeled considering the amount of H atoms forming CH–π interactions and the type of carboxylate closer to the surface. By counting the number of CH–π interactions, three types of structures can be distinguished, namely 0 H (relying only on anion–π interactions), 2 H, and 4 H. The carboxylate groups were sorted according to the presence of an O–Ru bond, or the presence of a negative charge (O^-). The molecular structures and their respective energy values were reported in Fig. S16 and Table S4.

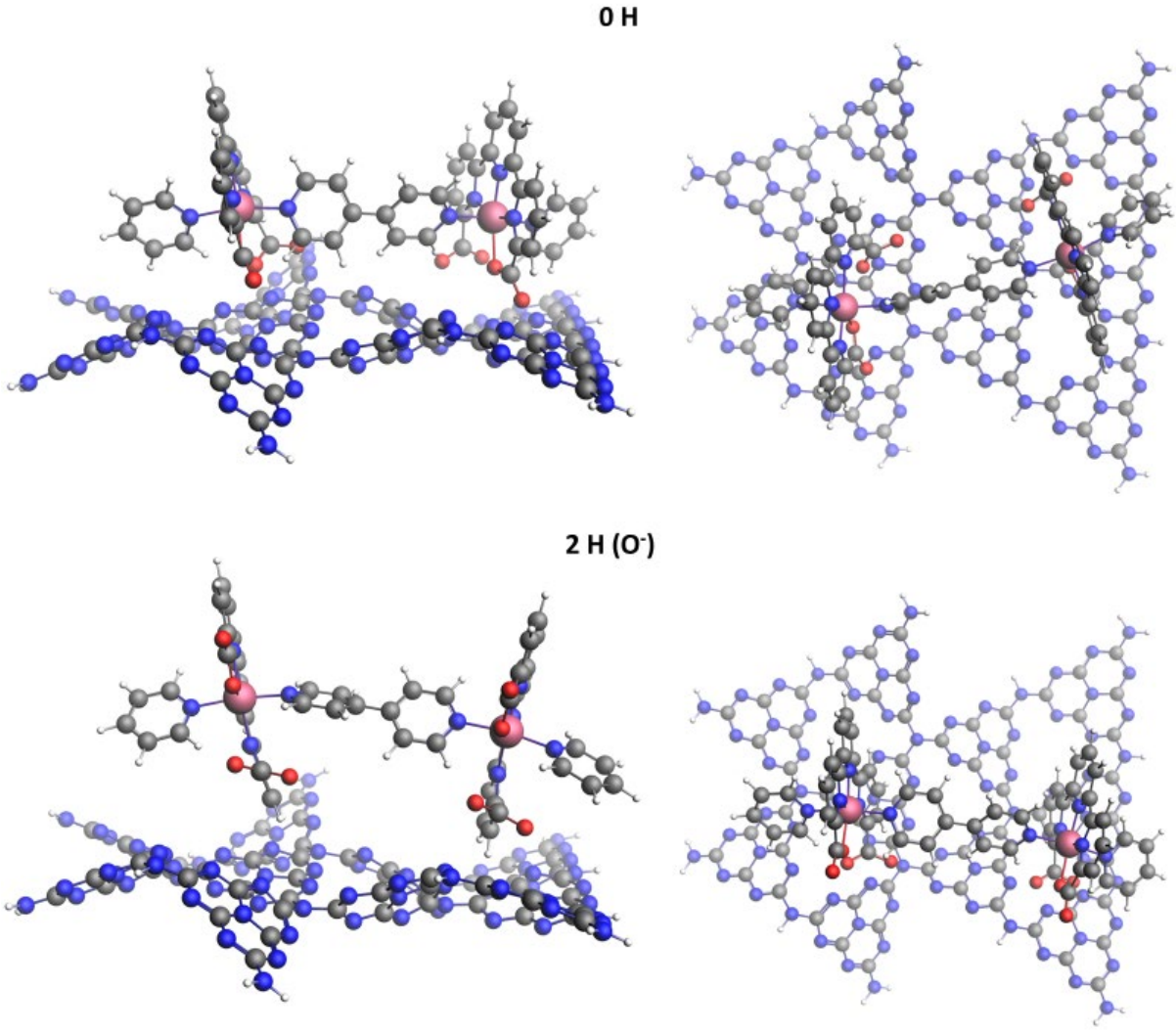

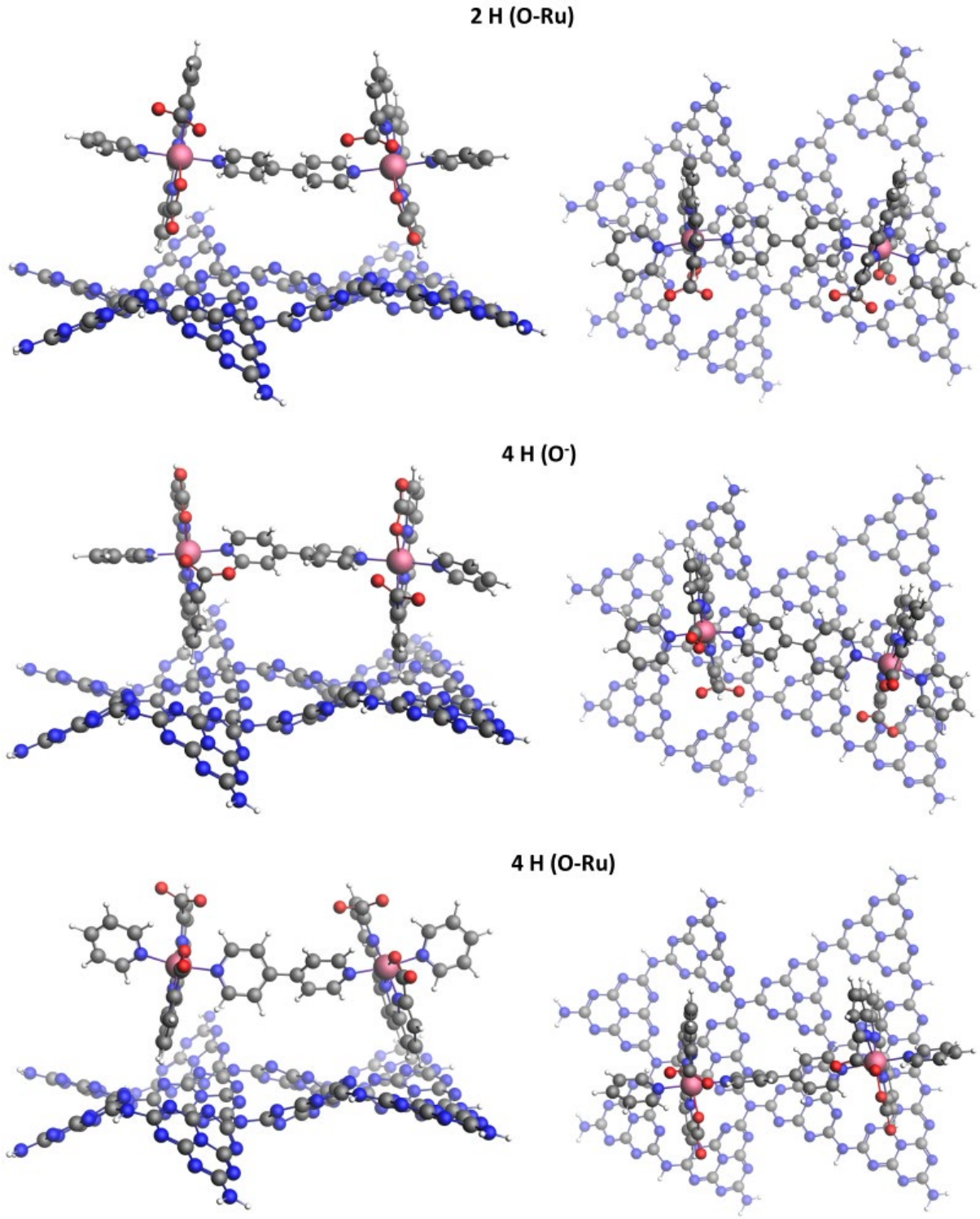

Fig. S16. Possible anchoring of Ru_2 on carbon nitride surface; (left) top views, (right) front views.

Table S4. Anchoring energies and Boltzmann distribution of the possible interacting geometries in water.

Attachment type	$E_{anchoring}$ (kcal mol^{-1})	E_{rel} (kcal mol^{-1})	Probability
0 H	–8.8	3.9	1.9×10^{-6}
2 H (O^-)	–4.1	8.6	2.9×10^{-13}
2 H (O–Ru)	–3.5	9.1	4.1×10^{-14}
4 H (O^-)	–12.7	0.0	1
4 H (O–Ru)	–10.8	1.9	1.5×10^{-3}

Table S5. Anchoring energies and Boltzmann distribution of the possible interacting geometries in water.

Attachment type	$E_{anchoring}$ (kcal mol^{-1})	E_{rel} (kcal mol^{-1})	Probability
0 H	–29.6	0.0	1
2 H (O^-)	–14.1	15.5	2.0×10^{-23}
2 H (O–Ru)	–9.9	19.7	1.3×10^{-29}
4 H (O^-)	–20.7	8.9	1.0×10^{-13}
4 H (O–Ru)	–19.9	9.7	6.5×10^{-15}

The inversion of the most stabilizing interaction becomes apparent when comparing the anchoring energies in solution with those in the gas phase. Indeed, when the system is not surrounded by solvent with which it could produce electrostatic interactions, the most stable interaction is the 0 H due to the formation of strong anion–π interactions with the surface. When water is taken into account implicitly, the electrostatic effect on the carboxylic groups leads to a diminishment of anion–π strength, bringing the four CH–π interactions of the 4 H (O^-) structure (with the additional stabilization of the carboxylic groups by the solvent) to be the most stable. It is worth noticing that a more accurate model using explicit water molecules would probably enhance the stability of system 4 H (O^-) due to the additional formation of hydrogen bonds with the solvent. The action of hydrophobic effect is to exclude because of the lower anchoring energies when the solvent is considered part of the system.

Besides this inversion for the most stabilizing interaction, two other trends are visible from our data. First of all, the anchoring via four CH–π interactions always leads to higher stability. Secondly, the anchoring via a structure with the dangling carboxylate closer to the surface is always to prefer over structures with the O–Ru

carboxylate closer. Even though the former claim is intuitive, the latter is not and deserves an explanation. The cause lies in the closer position of the pyridine to the dangling carboxylate when the dangling carboxylate is closer to the surface.

The CH–π distances in water phase of structure 4 H (O^-) are 2.36 and 3.26 Å for tda(1), and 2.85 and 3.08 Å for tda(2).

The anchoring energy for each dimeric structure considered ($E_{\text{anchoring dimer}}$) were calculated by the formula:

$$E_{\text{ancoring dimer}} = E_{\text{dimer on CN}} - (E_{\text{dimer}} + E_{\text{CN}}) \quad \text{(S6)}$$

Where $E_{\text{dimer on CN}}$ is the energy of the assembled system, and E_{dimer} and E_{CN} are the energies of the isolated dimer and surface, respectively.

These values were divided by two to determine the anchoring energy of each single Ru(tda)py_2 unit:

$$E_{\text{ancoring}} = \frac{E_{\text{ancoring dimer}}}{2} \quad \text{(S7)}$$

The relative energies (E_{rel}) were calculated as energy differences to the most stable anchoring ($E_{4\text{ H (O–)}}$) employing the Equation S8 for aqueous phase, or S9 for gas phase:

$$E_{\text{rel}} = E_i - E_{4\text{ H O}^-} \quad \text{(S8)}$$

$$E_{\text{rel}} = E_i - E_{0\text{ H}} \quad \text{(S9)}$$

Where in both cases, E_i is the energy of the anchoring to compare.

The Boltzmann distribution was obtained by Equation S10:

$$p_i = \frac{\exp(-\varepsilon_i/(k_{\text{B}}T))}{\sum \exp(-\varepsilon_j/(k_{\text{B}}T))} \quad \text{(S10)}$$

Where p_i is the probability of i-th interaction to take place, ε_i is the anchoring energy of the geometry under examination and ε_j are all the anchoring energies. The temperature was considered constant at 298.15 K.

The anchoring energy of an oligomer of 15 units of Ru(tda) was obtained multiplying the number of units (n units) times the anchoring energy of a single monomer ($E_{\text{anchoring}}$) using Equation S11:

$$E_{\text{ancoring oligomer 15}} = 15 \cdot E_{\text{anchoring}} \quad \text{(S11)}$$

Carbon nitride structure insights:

The structure of carbon nitride has long been debated. Many examples available in the literature overlook the true structural nature of carbon nitride and just consider it a planar surface.[25–27] However, recent studies aimed to clarify the topology of this

material showed that the most stable conformer possesses a certain degree of rugosity.[22,23,28–30] Here we want to provide some insights emerging from our calculations.

In our study we optimized a molecule of carbon nitride (CN10) by (i) leaving it able to adjust to its minimum energy and (ii) imposing a planar structure. The optimization lacking constraints led to a corrugated structure (in agreement with previous works[22,23,28–30]) being 154.6 kcal mol^{-1} more stable than its planar analog.

The lack of planarity was analyzed by measuring the dihedral angles of the N atoms connecting the heptazine units. A dihedral angle is the angle between two intersecting planes. In this case the planes are defined according to the atoms bound to the out-of-heptazines nitrogen, three types of nitrogen atoms can be distinguished, namely $ArNH_2$, Ar_2NH, and Ar_3N (see Fig. S17). The values of the dihedral angles are reported in Tables S5, S6, and S7.

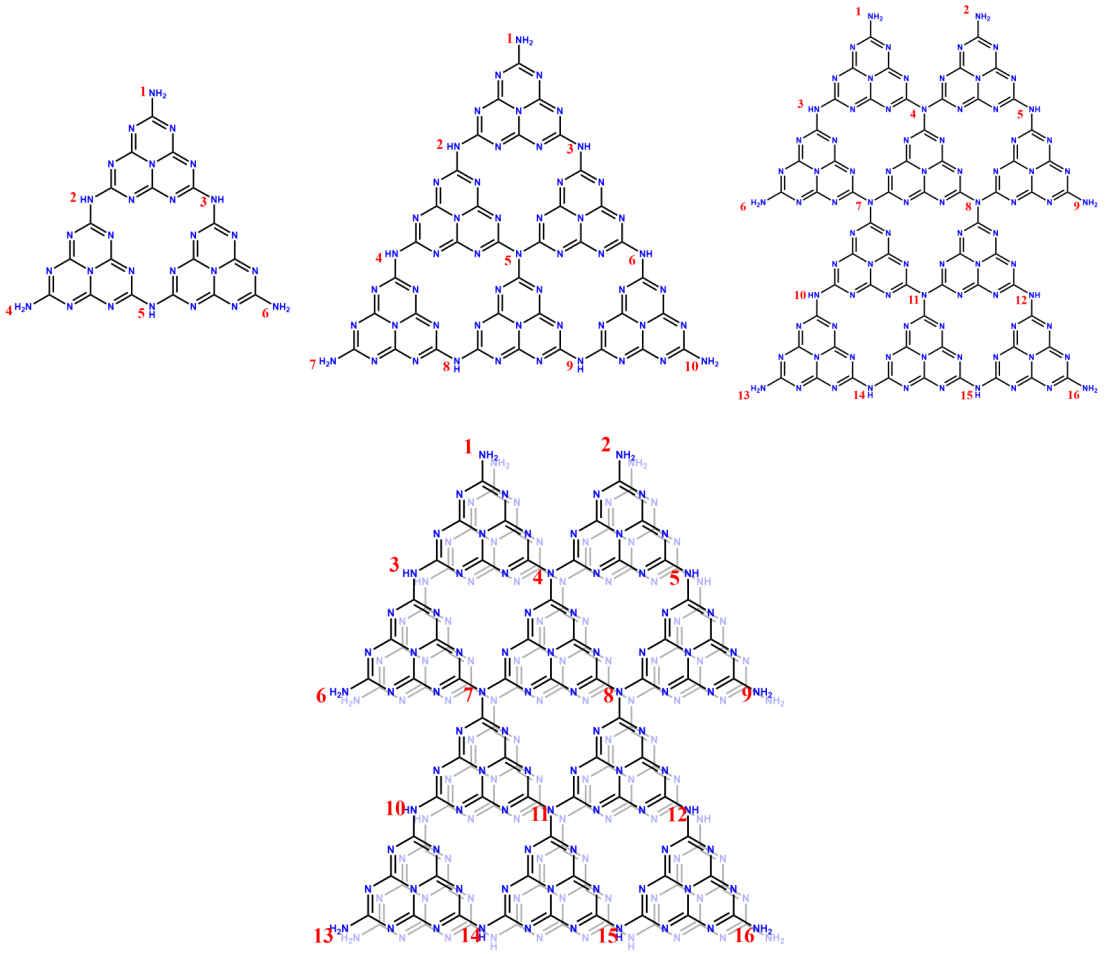

Fig. S17. Schematic representation of the carbon nitride models considered in this study CN3 (top left), CN6 (top center), CN10 (top right), and CN10 2 layers (bottom) with labeled N bridging atoms.

Table S6. Dihedral angles in the optimized structure of CN3.

$ArNH_2$	Dihedral angle
1	179.9°
4	156.6°
6	156.3°
Ar_2NH	**Dihedral angle**
2	192.5°
3	193.9°
5	180.6°

Table S7. Dihedral angles in the optimized structure of CN6.

$ArNH_2$	Dihedral angle
1	179.7°
7	180.0°
10	179.9°
Ar_2NH	**Dihedral angle**
2	167.3°
3	165.9°
4	153.6°
6	153.3°
8	177.7°
9	178.8°
Ar_3N	**Dihedral angle**
5	180.6°

Table S8. Dihedral angles in the optimized structure of CN10.

$ArNH_2$	Dihedral angle
1	174.2°
2	174.7°
6	177.1°
9	176.6°
13	178.0°
16	177.8°
Ar_2NH	**Dihedral angle**
3	139.2°
5	139.3°
10	151.7°
12	152.5°
14	178.3°
15	176.9°
Ar_3N	**Dihedral angle**
4	180.2°
7	167.2°
8	166.6°
11	177.7°

Table S9. Dihedral angles in the optimized structure of CN10 2 layers.

$ArNH_2$	Dihedral angle
1’	147.9°
2’	150.1°
6’	145.4°
9’	162.3°
13’	148.8°
16’	155.0°
1’’	147.9°
2’’	150.0°
6’’	153.3°
9’’	148.0°
13’’	148.6°
16’’	154.8°
Ar_2NH	**Dihedral angle**
3’	172.8°
5’	165.5°
10’	175.7°
12’	175.8°
14’	176.8°
15’	178.5°
3’’	169.5°
5’’	169.3°
10’’	175.7°
12’’	175.4°
14’’	178.7°
15’’	177.0°
Ar_3N	**Dihedral angle**
4’	175.9°
7’	175.0°
8’	175.5°
11’	173.6°

4''	178.4°
7''	176.5°
8''	175.9°
11''	175.4°

The distortion from planarity was defined by the Equation S12:

$$\text{deviation from planarity (°)} = 180\,° - \text{dihedral angle (°)} \qquad \text{(S12)}$$

Where the dihedral angles considered are the angles formed by the bridging N atoms.

It is noteworthy that the average deviation for Ar_3N in CN10 is 7.2°, while this value decreases to 5° and 3.5° for the two layers of CN10 2 layers. This data clearly shows that the interlayer π–π stacking helps the planarity of the system and that the distortion present in the CN10 model is slightly exaggerated by the lack of additional layers.

In the bridging N, surrounded exclusively by aromatic systems, the maximum distortion from planarity is produced in CN10 2 layers with a value of 173.6° (180° – 173.6° = 6.4°) (see Fig. S18). In both cases, the deviation from planarity is modest and allows a π-conjugation over the entire surface, in agreement with a previous report.[31]

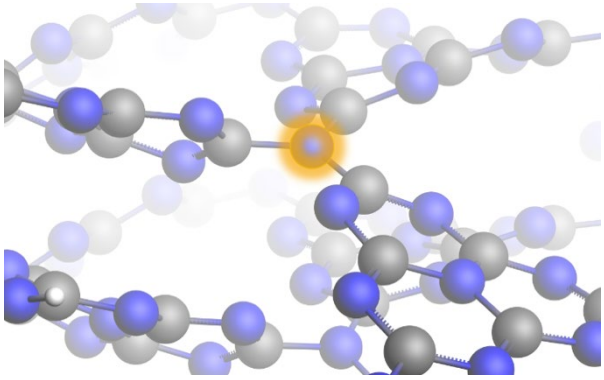

Fig. S18. View of a bridging N atom in CN10 2 layers (highlighted with an orange hue).

Even though these conclusions might appear contradictory to the hypothesis of a planar material, the partial sp^3 character of the bridging N is not the main reason for the lack of planarity. The fundamental cause for the non-planarity of the carbon nitride is attributed to the repulsion produced between the neighboring N atoms belonging to the different heptazine units, leading to a distortion to alleviate the tension. A graphical description of these repulsive forces is reported in Fig. S19.

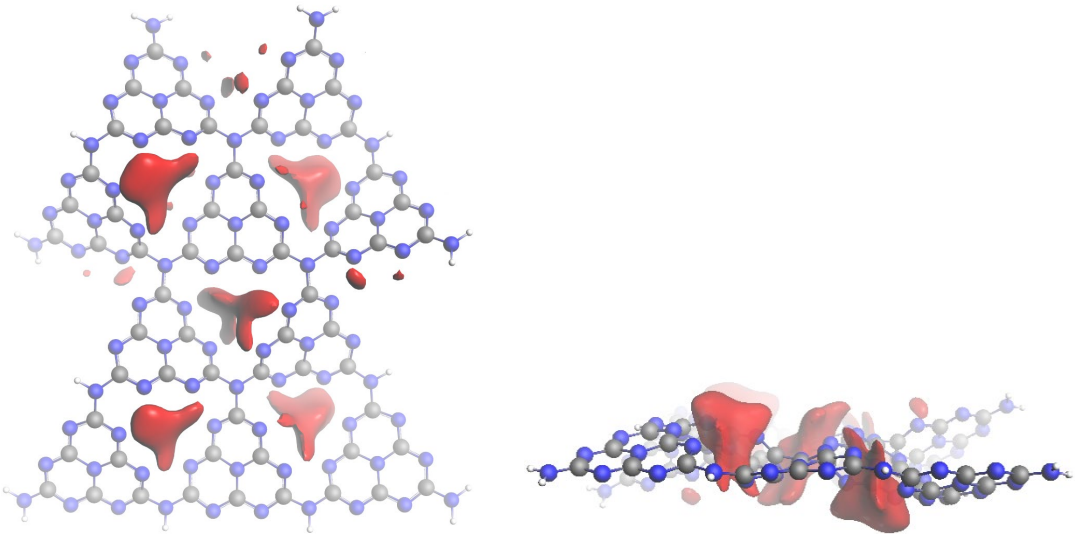

Fig. S19. Coulombic potential SCF (in red) in CN10: (left) top view, (right) side view.

Photoexcitation:

To gain some insights on the processes occurring upon light excitation of the system, we computed the absorption spectra by means of TD-DFT. Fig. S20 reports the spectra of the two-separate species, namely the surface (CN_{Red}) and the oligomer, and of the assembled system. It is worth noting that the band emerging in the assembled system at 500–650 nm does not derive from the overlap of absorption of its components, but it is rather a consequence of the assembly. The only possible reason for this new band to emerge is the direct electron excitation from one component to another. This mechanism differs from the more common electron transfer mechanism, in which the electron gets promoted to the excited state of the photosensitizer and subsequently undergoes electron transfer to the acceptor.

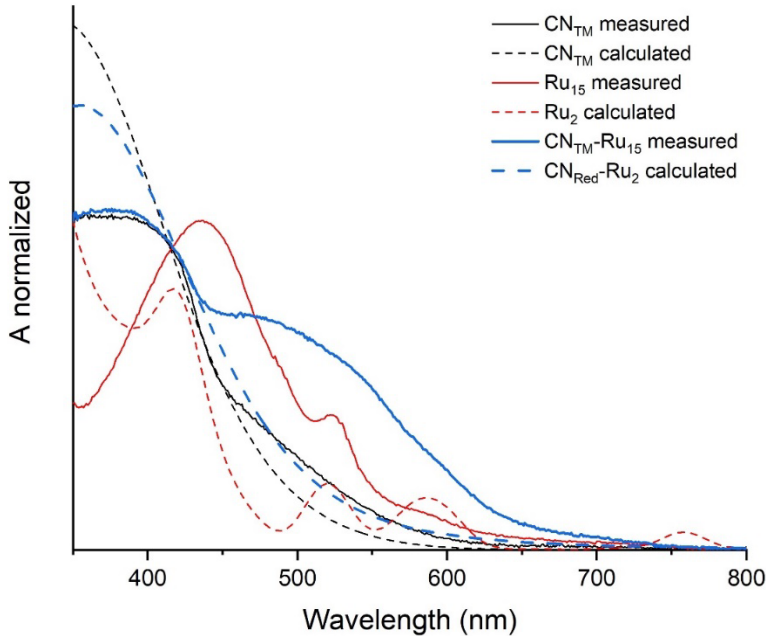

Fig. S20. Measured (solid lines) and calculated (dashed lines) UV–vis spectra.

The plateau reached near 400 nm in the measured spectra of **CN_{TM}** and **CN_{TM}–Ru_{15}** represents the saturation due to the absorption of all incident photons. This effect is not observed in the simulated spectra as the excitation method cannot produce saturation.

To better comprehend the nature of the newly emerged band (500–650 nm), the orbitals involved in its main transitions are shown in Fig. S21. All these transitions describe the excitation of an electron localized on the Ru(tda) unit to the carbon nitride, indicating a complex-to-surface electron transfer. These results are in agreement with the arising of the new band.

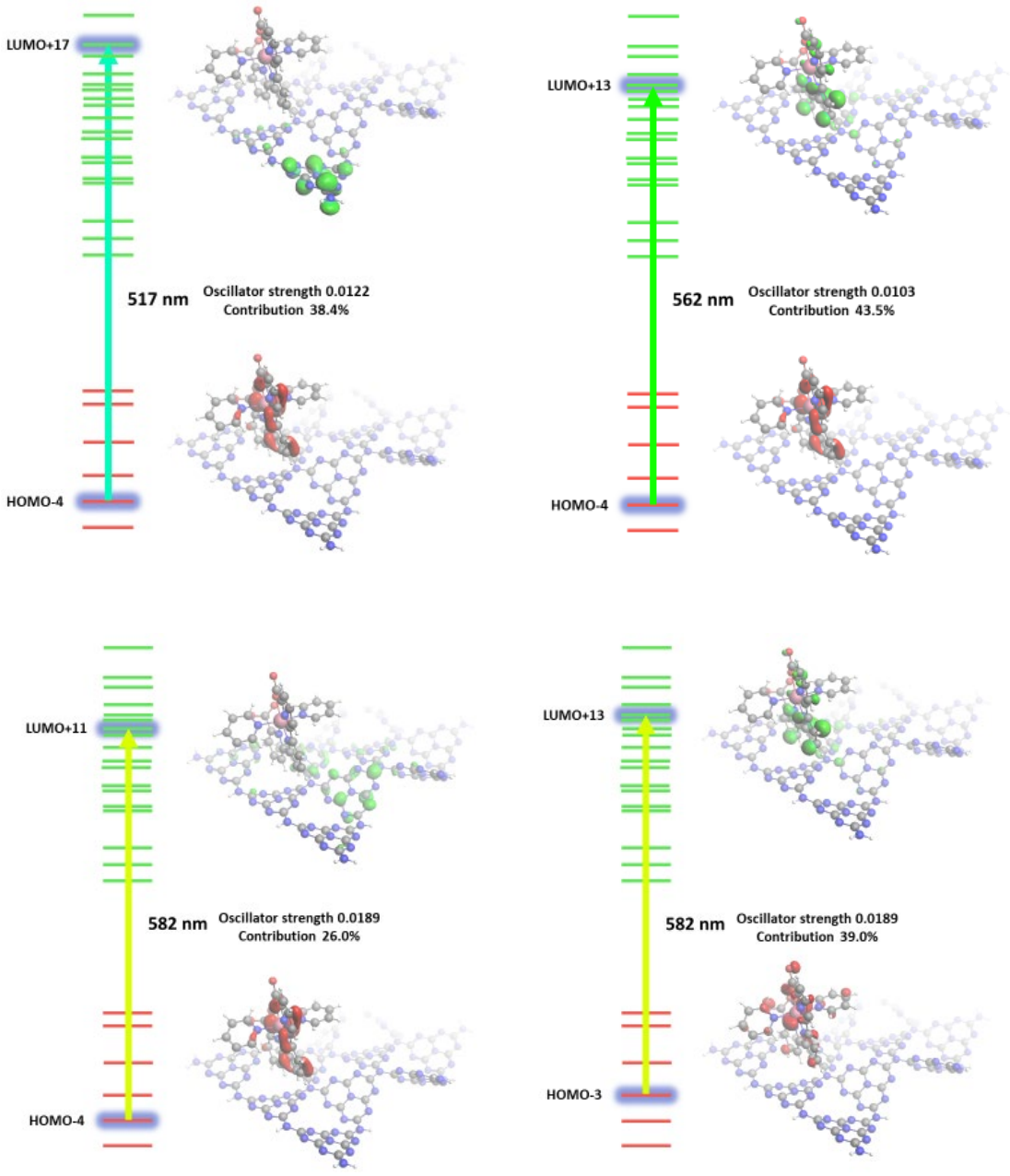

Fig. S21. Major contributions for the transition at 517 nm, 562 nm, and 582 nm. The orbitals and energy levels are depicted in red (populated) and green (excited).

Moreover, the measured and simulated UV–vis spectra of **CN_{TM}** and the oligomer of ruthenium were plotted individually to provide more details on the separated systems (Fig. S22). All the spectra were normalized to provide a good fitting of the calculated oscillator strength with the measured absorbance.

In the case of **CN_{TM}**, the simulation follows the trend of the measured spectrum. However, the theoretical and experimental spectra diverge in the region

below 400 nm. The experimental spectrum shows saturation caused by the absorption of all the incident photons. On the other hand, the calculations cannot reach a saturation state, i.e., in this region, the intensity is remarkably enhanced due to all the high energy transitions.

The absorption of the oligomer (Ru_{15}) was described using a dimeric model (Ru_2). The simulated trend of Ru_2 fits the experimental spectrum of the 15 units oligomer. It is noteworthy that the peak at 437 nm of **Ru_{15}** is blue-shifted in the Ru_2 model at 417 nm. This difference is not the consequence of an inappropriate model but the fruit of a constant red-shift taking place from the monomer to the pentadecamer, already described in a previous work.[4]

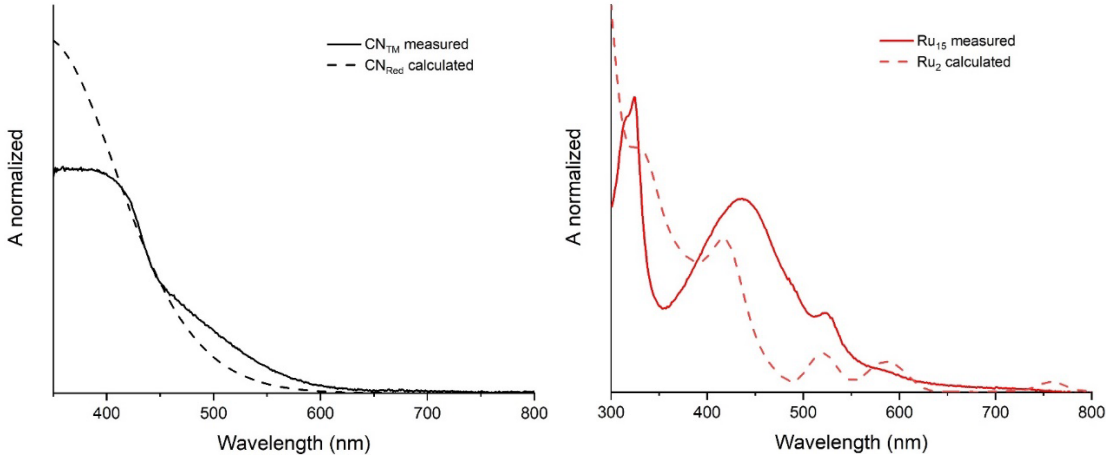

Fig. S22. Measured (solid line) and calculated (dashed line) UV–vis spectra of CN (left) and Ru oligomer (right).

Electronic Supplementary Information References

1 R. Matheu, J. Benet-Buchholz, X. Sala and A. Llobet, *Inorg. Chem.*, 2018, **57**, 1757–1765.

2 T. Shmila, S. Mondal, S. Barzilai, N. Karjule, M. Volokh and M. Shalom, *Small*, 2023, **19**, 2303602.

3 J. Qin, J. Barrio, G. Peng, J. Tzadikov, L. Abisdris, M. Volokh and M. Shalom, *Nat. Commun.*, 2020, **11**, 4701.

4 M. A. Hoque, M. Gil-Sepulcre, A. de Aguirre, J. A. A. W. Elemans, D. Moonshiram, R. Matheu, Y. Shi, J. Benet-Buchholz, X. Sala, M. Malfois, E. Solano, J. Lim, A. Garzón-Manjón, C. Scheu, M. Lanza, F. Maseras, C. Gimbert-Suriñach and A. Llobet, *Nat. Chem.*, 2020, **12**, 1060–1066.

5 G. t Te Velde, F. M. Bickelhaupt, E. J. Baerends, C. Fonseca Guerra, S. J. A. van Gisbergen, J. G. Snijders and T. Ziegler, *J. Comput. Chem.*, 2001, **22**, 931–967.

6 A. D. Becke, *Phys. Rev. A*, 1988, **38**, 3098.

7 J. P. Perdew and W. Yue, *Phys. Rev. B*, 1986, **33**, 8800.

8 E. Caldeweyher, S. Ehlert, A. Hansen, H. Neugebauer, S. Spicher, C. Bannwarth and S. Grimme, *J. Chem. Phys.* 2019, **150**.

9 E. van Lenthe, E.-J. Baerends and J. G. Snijders, *J. Chem. Phys.*, 1993, **99**, 4597–4610.

10 E. Van Lenthe, A. Ehlers and E.-J. Baerends, *J. Chem. Phys.*, 1999, **110**, 8943–8953.

11 A. Klamt, *J. Phys. Chem.*, 1995, **99**, 2224–2235.

12 C. C. Pye and T. Ziegler, *Theor. Chem. Acc.*, 1999, **101**, 396–408.

13 J. Heyd, G. E. Scuseria and M. Ernzerhof, *J. Chem. Phys.*, 2003, **118**, 8207–8215.

14 P. R. T. Schipper, O. V Gritsenko, S. J. A. van Gisbergen and E. J. Baerends, *J. Chem. Phys.*, 2000, **112**, 1344–1352.

15 O. V Gritsenko, P. R. T. Schipper and E. J. Baerends, *Chem. Phys. Lett.*, 1999, **302**, 199–207.

16 M. Álvarez-Moreno, C. de Graaf, N. Lopez, F. Maseras, J. M. Poblet and C. Bo, *J. Chem. Inf. Model.*, 2015, **55**, 95–103.

17 J. Li, X. Wang, L. Huang, L. Tian, M. Shalom, C. Xiong, H. Zhang, Q. Jia, S. Zhang and F. Liang, *Nanoscale*, 2021, **13**, 12634–12641.

18 N. Karjule, C. Singh, J. Barrio, J. Tzadikov, I. Liberman, M. Volokh, E. Palomares, I. Hod and M. Shalom, *Adv. Funct. Mater.*, 2021, **31**, 2101724.

19 R. Gong, D. Mitoraj, D. Gao, M. Mundszinger, D. Sorsche, U. Kaiser, C. Streb, R. Beranek and S. Rau, *Adv. Sustain. Syst.*, 2022, **6**, 2100473.

20 W. Zhang, J. Albero, L. Xi, K. M. Lange, H. Garcia, X. Wang and M. Shalom, *ACS Appl. Mater. Interfaces*, 2017, **9**, 32667–32677.

21 Y. Hou, F. Zuo, A. P. Dagg, J. Liu and P. Feng, *Adv. Mater.*, 2014, **26**, 5043–5049.

22 J. Sehnert, K. Baerwinkel and J. Senker, *J. Phys. Chem. B*, 2007, **111**, 10671–10680.

23 J. Wang, D. Hao, J. Ye and N. Umezawa, *Chem. Mater.*, 2017, **29**, 2694–2707.

24 A. Galushchinskiy, Y. Zou, J. Odutola, P. Nikačević, J. Shi, N. Tkachenko, N. López, P. Farràs and O. Savateev, *Angew. Chem. Int. Ed.*, 2023, **62**, e202301815.

25 X. Wang, J. Ma, J. Fan, H. Zhu, X. Liu, H. Xia and Y. Liu, *J. Chem. Inf. Model.*, 2023, **63**, 4708–4715.

26 X. Wang, S. Blechert and M. Antonietti, *Acs Catal.*, 2012, **2**, 1596–1606.

27 H.-Z. Wu, L.-M. Liu and S.-J. Zhao, *Phys. Chem. Chem. Phys.*, 2014, **16**, 3299–3304.

28 L. M. Azofra, D. R. MacFarlane and C. Sun, *Phys. Chem. Chem. Phys.*, 2016, **18**, 18507–18514.

29 K. Asif, M. Perveen, R. A. Khera, S. Nazir, A. R. Ayub, T. Asif, M. Shabbir and J. Iqbal, *Comput. Theor. Chem.*, 2021, **1206**, 113459.

30 S. Melissen, T. Le Bahers, S. N. Steinmann and P. Sautet, *J. Phys. Chem. C*, 2015, **119**, 25188–25196.

31 S. Cao, J. Low, J. Yu and M. Jaroniec, *Adv. Mater.*, 2015, **27**, 2150–2176.